Photoacoustics 19 (2020) 100175

Contents lists available at ScienceDirect

Photoacoustics

journal homepage: www.elsevier.com/locate/pacs

Research article

Photoacoustic reconstruction from photothermal measurements including prior information

G. Thummerer[a,*], G. Mayr[a], M. Haltmeier[b], P. Burgholzer[c]

[a] Josef Ressel Centre for Thermal NDE of Composites, University of Applied Sciences Upper Austria, Wels, Austria
[b] Department of Mathematics, University of Innsbruck, Innsbruck, Austria
[c] RECENDT – Research Centre for Nondestructive Testing, Linz, Austria

ARTICLE INFO

Keywords:
Thermography
Photoacoustic PDE
Inverse problem
Regularization
Image reconstruction

ABSTRACT

Photothermal measurements with an infrared camera enable a fast and contactless part inspection. The main drawback of existing reconstruction methods is the degradation of the spatial resolution with increasing imaging depth, which results in blurred images for deeper lying structures. In this paper, we propose an efficient image reconstruction strategy that allows prior information to be included to overcome the diffusion-based information loss. Following the virtual wave concept, in a first step we reconstruct an acoustic wave field that satisfies the standard wave equation. Therefore, in the second step, stable and efficient reconstruction methods developed for photoacoustic tomography can be used. We compensate for the loss of information in thermal measurements by incorporating the prior information positivity and sparsity. Therefore, we combine circular projections with an iterative regularization scheme. Using simulated and experimental data, this work demonstrates that the quality of the reconstruction from photothermal measurements can be significantly enhanced.

1. Introduction

Photoacoustic (or optoacoustic) tomography uses thermoelastic expansion following a rapid temperature rise after the illumination of light absorbing structures within a semitransparent and turbid material, such as a biological tissue. Photothermal imaging belongs to the methods of active thermography and measures directly the increased temperature propagating by heat diffusion from the light absorbing structures to the surface of the sample. Both methods have the same optical absorption contrast and enable to detect hemoglobin, lipids, water and other light-absorbing chromophores, but with greater penetration depth than purely optical imaging modalities that rely on ballistic photons [1–3]. In photoacoustic tomography, the temporal evolution of the acoustic pressure field is sampled using an array of ultrasound detectors placed on the tissue surface or by moving a single detector across the detection surface. From the measured pressure signals, images of the optical absorption within the tissue can be reconstructed by time reversal and back projection methods or by solving an inverse source problem [3–5]. In photothermal imaging the surface temperature evolution is measured by an infrared camera.

The achievable spatial resolution for photoacoustic tomography and photothermal imaging degrades with imaging depth, which results in blurred images of deeper lying structures. Besides pure technical limitations of the measurement equipment, the ultimate resolution limit has its origin in the second law of thermodynamics: scattering, dissipation or diffusion of the acoustic or “thermal” wave on its path through the sample causes entropy production, which is equal to the loss of information [6–8] (Fig. 1). As the information content of the reconstructed image strongly correlates with the spatial resolution, the higher entropy production from deeper lying structures causes a degradation in resolution. Overcoming the resolution limit due to entropy production is not trivial. Without taking into account additional knowledge or information about the sample, no mathematical reconstruction algorithm can compensate for this information loss, causing the degradation in resolution.

Super-resolution fluorescence imaging techniques, such as stochastic optical reconstruction microscopy (STORM) [9], photoactivated localization microscopy (PALM) [10], or super-resolution optical fluctuation imaging (SOFI) [11] utilize the fact that the localization of point sources (e.g. activated florescent molecules) is possible with a much higher accuracy than the width of the point spread function (PSF). Although the resolution in optical imaging has been greatly improved, there continues to be rapid advancements in the development of high resolution imaging methods also for many other imaging modalities. Localization microscopy was also used to achieve super-resolution in ultrasound imaging by using scattering microbubbles instead of

* Corresponding author.
E-mail address: Gregor.Thummerer@fh-wels.at (G. Thummerer).

https://doi.org/10.1016/j.pacs.2020.100175
Received 6 November 2019; Received in revised form 31 January 2020; Accepted 8 March 2020
Available online 19 March 2020

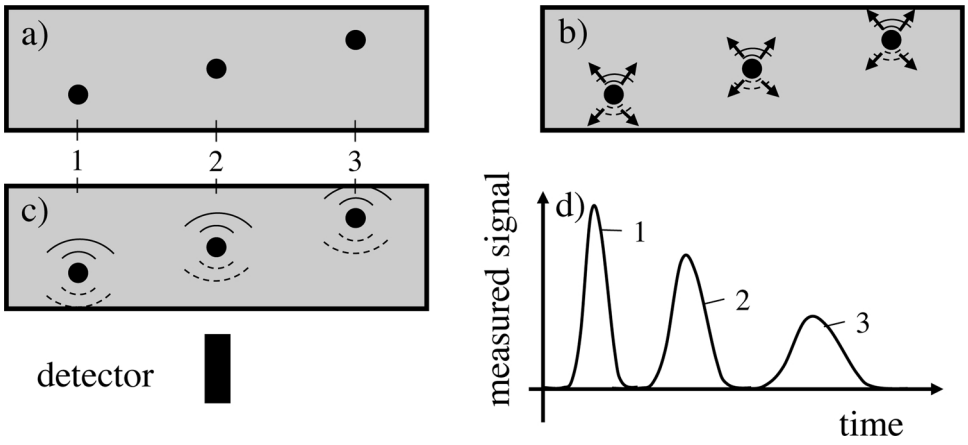

Fig. 1. Schematic sketch of the information loss from entropy production during scattering, dissipation, or diffusion. (a) Sample with subsurface structure, which should be imaged; (b) propagation of the acoustic or "thermal" waves to the sample surface: entropy production determines the loss of information; (c) detection of signals at the sample surface; (d) measured signals at the detector surface as a function of time. Due to entropy production, the signal from the deeper structures has not only a smaller amplitude. They are also broadened compared to the signal from the structure just beneath the surface.

fluorescent molecules as point sources [12,13], and recently even for in vivo localization of single dyed droplets for photoacoustic tomography [14]. Ultrafast localization microscopy allows for super-resolution ultrasound imaging of vasculature in whole organs [15].

In the field of optics, it has been known since 2007 that optical diffusion in a strong scattering sample can be "inverted" by wavefront shaping [16]. Coherent photons from a laser scatter in a deterministic way (at least for a certain correlation time), which is measured pointwise. The resulting scattering matrix is used to change the light wave front, e.g. by a spatial light modulator in such a way that after diffusive scattering the light is focused. For heat diffusion, phonons are not coherent and the propagation of phonons is highly uncorrelated in time. Therefore, a "phonon scattering matrix" cannot be measured and used to invert heat diffusion in time. For photoacoustic imaging in a (quasi) diffusive regime a comprehensive overview about the advances in super-resolution imaging was recently given by Shi et al. [17].

The degradation of spatial resolution with increasing imaging depth in thermographic imaging could be circumvented by using structured heating, e. g. by structured illumination patterns. For super-resolution reconstruction out of numerous images with different illumination patterns, we have successfully proposed a non-linear iterative joint sparsity (IJOSP) algorithm [18,19].

These patterns can even be unknown, which is called blind structured illumination. We demonstrated this by imaging a line pattern and a star-shaped structure through a metal sheet with a resolution that was four times better than the resolution limit from entropy production [19]. The structured illumination was realized using parallel slits cut in an aluminum foil, where the excitation is carried out either by a flash lamp, which passes through the slits in the foil, or by a high-power laser with a line-shaped spot.

In this work, we demonstrate that even without structured illumination, just by taking into account prior information, such as positivity and sparsity of the heated structures inside the sample and using adequate iterative non-linear reconstruction algorithms, the increased blurring with imaging depth can be reduced significantly. Positivity comes from the fact that heating always causes a temperature increase. By converting the temperature signal into a virtual wave, which is a solution of the wave equation, positivity is not directly preserved for 2D and 3D wave propagation. An initially nonnegative acoustic signal will take negative values during propagation. In this work, we account for this issue by calculating the circular or spherical projections, which is in 2D the Abel transformation and in 3D the time integral of the virtual wave [20]. The circular and spherical projections preserve positivity of the initial source. For one data point the information gain by a positivity constraint would be only a factor of two, but for a signal with n data points this factor becomes 2^n, which can be large for higher n. More information could be gained by using also sparsity. Sparsity can often be assumed because defects, such as cracks in samples, are usually sparse and also in biomedical imaging the sample consists of different types of tissues separated by "sparse" interfaces. The application of the virtual wave concept (VWC) with prior information for a high-resolution thermographic image reconstruction is shown using 2D experimental surface temperature data.

2. Virtual wave concept

The intention of the virtual wave concept is to reconstruct the initial temperature distribution $T_0(\mathbf{r})$ based on temporal temperature data $T(\mathbf{r}, t)$ measured at the sample surface (Fig. 2a, c). For this purpose, we transform $T(\mathbf{r}, t)$ locally into a virtual wave field $T_{\text{virt}}(\mathbf{r}, t)$ (Fig. 2d) in order to enable the application of efficient and stable photoacoustic image reconstruction methods. The reconstruction of the initial heat sources is imaged in Fig. 2e.

2.1. Forward problem

The direct or forward problem is analytically given by the heat equation

$$\left(\nabla^2 - \frac{1}{\alpha}\frac{\partial}{\partial t}\right) T(\mathbf{r}, t) = -\frac{1}{\alpha} T_0(\mathbf{r})\delta(t). \tag{1}$$

The heat equation describes the heat diffusion process in a solid and hence the temperature distribution $T(\mathbf{r}, t)$ as function of position vector $\mathbf{r} = (x, y, z)$, where x, y, z are the Cartesian coordinates, and time t. α is the thermal diffusivity. The right hand side of Eq. (1) represents the source term. Herein, the temporal *Dirac-Delta* distribution $\delta(t)$ arranges that the spatial temperature distribution $T_0(\mathbf{r})$ is introduced at time $t = 0$. The heat equation can be classified as parabolic partial differential equation (PDE) and describes an irreversible process. Practically the forward problem is given by heating up the test specimen, e.g. by absorption of optical radiation or induction of eddy current and measuring the corresponding temporal temperature change at the surface. In Fig. 2a an exemplary initial temperature distribution is illustrated. The corresponding simulated surface temperature distribution $T(y, z = 0)$ is imaged in Fig. 2c.

The propagation of the virtual wave $T_{\text{virt}}(\mathbf{r}, t')$ is based on the acoustic wave equation for pressure [21]

$$\left(\nabla^2 - \frac{1}{c^2}\frac{\partial^2}{\partial t^2}\right) p(\mathbf{r}, t) = -\frac{1}{c^2}\frac{\partial}{\partial t} p_0(\mathbf{r})\delta(t). \tag{2}$$

Herein, $p(\mathbf{r}, t)$ is the photoacoustic wave pressure, $p_0(\mathbf{r})$ is the initial pressure distribution and c is the speed of sound. We claim, that the following initial pressure and temperature distribution relation holds:

$$p(\mathbf{r}, t = 0) = p_0(\mathbf{r}) = c^2\rho\beta T_0(\mathbf{r}) \quad \text{for} \quad t = 0, \tag{3}$$

where ρ is the material density and β is the thermal expansion

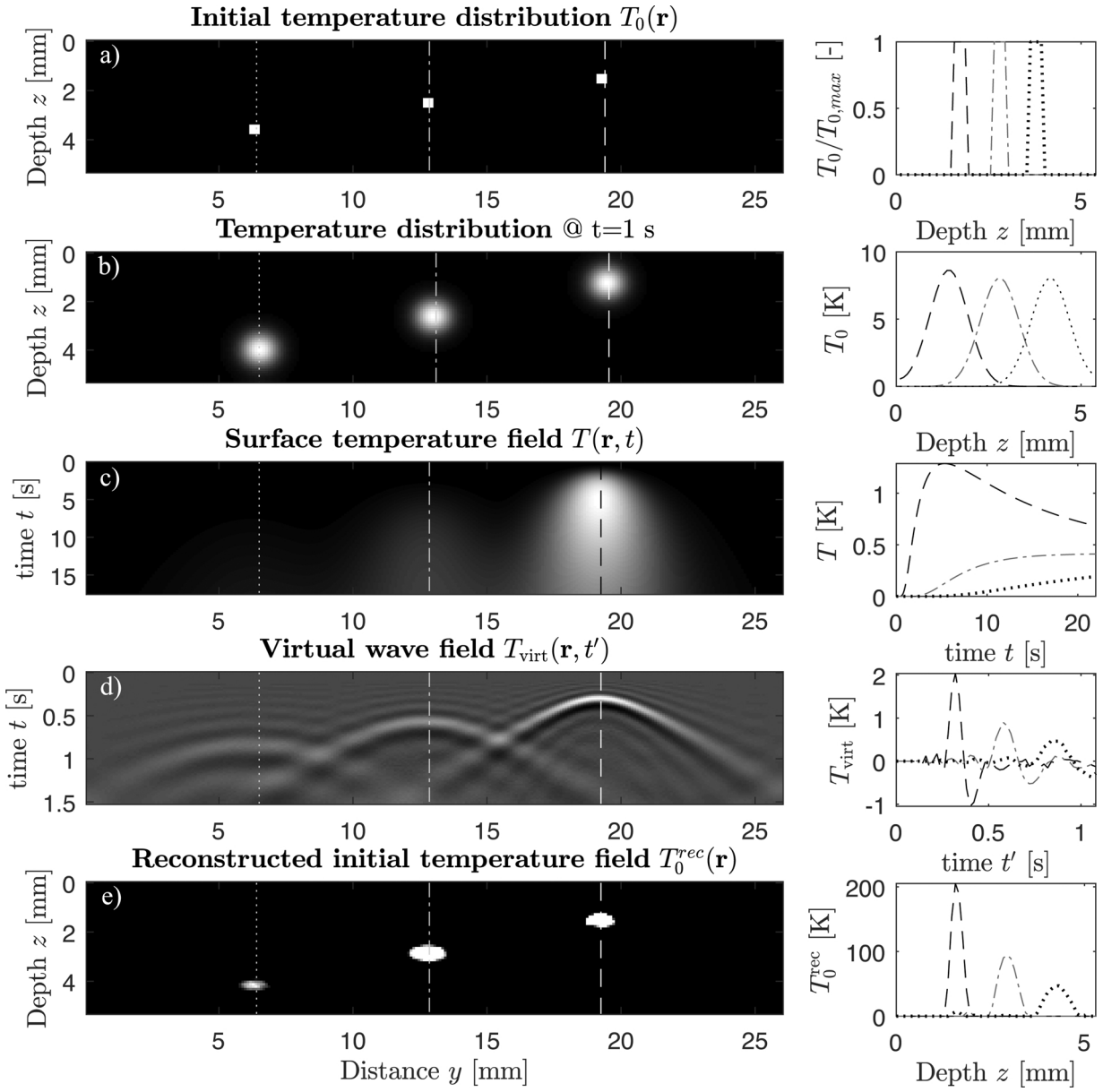

Fig. 2. Process steps of VWC based on simulated data with internal heat sources: (a) initial temperature distribution 2D (left) and 1D (right) at y = {6.5,13,19.5} mm, (b) spatial temperature distribution at t = 1 s, (c) simulated surface temperature field, (d) virtual wave field and (e) reconstructed field.

coefficient of the observed material. Then we define a virtual wave field, where the above relationship is extended for times $t > 0$ by introducing the virtual time scale t':

$$T_{\text{virt}}(\mathbf{r}, t') = \frac{p(\mathbf{r}, t)}{c^2 \rho \beta}. \tag{4}$$

By substituting Eqs. (3) and (4) into the acoustic wave equation for pressure, Eq. (2), the PDE for the virtual wave propagation yields:

$$\left(\nabla^2 - \frac{1}{c^2}\frac{\partial^2}{\partial t'^2}\right) T_{\text{virt}}(\mathbf{r}, t') = -\frac{1}{c^2}\frac{\partial}{\partial t'} T_0(\mathbf{r})\delta(t'). \tag{5}$$

Herein, c is the virtual speed of sound and t' corresponds to the virtual time scale. The wave equation can be classified as hyperbolic PDE and is, in contrast to the heat equation, time reversible. The virtual wave exhibit wave properties such as wavefront propagation, reflection and refraction [22,23]. Frequency domain- synthetic aperture focusing technique (F-SAFT), a well known acoustic reconstruction method, is used to reconstruct the initial temperature distribution $T_0^{\text{rec}}(\mathbf{r})$. $T_0(\mathbf{r})$ is again the initial temperature distribution.

2.1.1. Fredholm integral equation

According to Burgholzer et al. [24] the temperature distribution $T(\mathbf{r}, t)$, can be calculated based on the virtual wave field $T_{\text{virt}}(\mathbf{r}, t')$ and the kernel $K(t, t')$ for the same position vector $\mathbf{r}$, but different time scales t and t':

$$T(\mathbf{r}, t) = \int_{-\infty}^{\infty} T_{\text{virt}}(\mathbf{r}, t') K(t, t') \mathrm{d}t' \tag{6}$$

with

$$K(t, t') = \frac{c}{\sqrt{\pi \alpha t}} \exp\left(-\frac{c^2 t'^2}{4\alpha t}\right) \quad t > 0. \tag{7}$$

The kernel, Eq. (7), contains the thermal diffusivity α and virtual speed of sound c, which are the characteristic parameters for heat and virtual wave propagation. Eqs. (6) and (7) are valid for a temporal *Dirac-Delta* like heating $h(t) = \delta(t)$ of the specimen. To obtain Eq. (7), we have to Fourier transform Eqs. (1) and (5) temporally. Due to the elimination of

the time derivatives one can find a relationship between temperature field and virtual wave field for the same position vector **r**. Applying the inverse Fourier transformation on this relationship yields Eq. (6) and consequently Eq. (7). Due to the linear nature of wave and diffusion equation, Eq. (6) can be extended for any heating function $h(t)$ via temporal convolution [6]. The benefit of VWC compared to the direct solution of the inverse heat conduction problem (IHCP) comes with the application on multidimensional heat conduction problems. Here the VWC, in contrast to IHCP where the temporal and spatial components are treated simultaneously, solves for the temporal virtual wave field which yields the depth information such as defect depth, front wall and backwall. This first reconstruction step is then post processed by acoustic reconstruction methods where again the temporal information and the spatial components are respected.

3. Image reconstruction

3.1. Inverse problem

Our goal is to convert the measured or simulated temperature field into a so-called virtual wave field to enable the application of photoacoustic reconstruction methods. As mentioned previously, a consequence of entropy production during heat diffusion, characterized by the heat equation is that information is lost. Hence, calculating T_{virt} from T is a severely ill-posed inverse problem and regularization tools are necessary to calculate an appropriate regularized solution [25].

Usually, thermographic data is discrete in time and space. Hence, it is convenient to write Eq. (6) in discrete matrix form with $t_k = (k-1)\Delta_t$ and $t'_j = (j-1)\Delta_{t'}$

$$\mathbf{T} = \mathbf{K}\mathbf{T}_{\text{virt}} \tag{8}$$

The matrices have the subsequent dimensions: $\mathbf{T} \in \mathbb{R}^{m\times q}$, $\mathbf{K} \in \mathbb{R}^{m\times n}$ and $\mathbf{T}_{\text{virt}} \in \mathbb{R}^{n\times q}$ with $k = \{1, 2, \ldots, m\}$ and $j = \{1, 2, \ldots, n\}$. The variable $\ell = \{1, 2, \ldots, q\}$, counts for the spatial extension in y. For a *Dirac-Delta* like heating function $h(t) = \delta(t)$, the components of the **K**-matrix are calculated in the following manner:

$$\begin{aligned} K_{\text{kj}} &= \frac{\tilde{c}}{\sqrt{\pi\Delta_{\text{Fo}}(k-1)}}\exp\left(-\frac{\tilde{c}^2(j-1)^2}{4\Delta_{\text{Fo}}(k-1)}\right) \\ &= \frac{\eta}{\sqrt{\pi(k-1)}}\exp\left(-\frac{\eta^2(j-1)^2}{4(k-1)}\right). \end{aligned} \tag{9}$$

During calculation of the matrix elements K_{kj} the expression (1/0) occurs for $k = 1$. Hence, the first row of the Kernel-matrix is set to zero: $\mathbf{K}(1, :) = \mathbf{0}$. In Eq. (9), the dimensionless numbers $\tilde{c}$, Δ_{Fo} and η are defined as

$$\tilde{c} = \frac{c\Delta_{t'}}{\Delta_y};\quad \Delta_{\text{Fo}} = \frac{\alpha\Delta_t}{\Delta_y^2};\quad \eta = \frac{\tilde{c}}{\sqrt{\Delta_{\text{Fo}}}}, \tag{10}$$

where $\tilde{c}$ equates to the *Courant-Friedrichs-Levy* (CFL) number [26], Δ_{Fo} is the discrete *Fourier* number [27] and η is the ratio of these dimensionless numbers.

3.1.1. Reduction to circular projections

The quality of the regularized solution, i.e. the solution of the virtual wave field can be enhanced if prior informations, such as positivity or sparsity, are available. Considering the temperature distribution based on a heating pulse, in all spatial dimensions, the temperature distribution is always positive with respect to the ambient temperature for each time step of the simulation or measurement data. In contrast to this, the virtual wave field is not positive for all spatial dimensions. Positivity of the virtual wave field can only be guaranteed if the reconstruction is based on a one dimensional heat conduction problem. Hence, the intention is to transfer the multidimensional virtual wave data, via circular projections into a positive data set in order to incorporate the additional condition positivity [20,28,29]. Therefore, we consider the circular projection $\mathbf{M}_{\text{virt}}$ which can be computed with the inverse Abel transformation of the two dimensional virtual wave field $\mathbf{T}_{\text{virt}}$:

$$\mathbf{M}_{\text{virt}} = \mathbf{A}^{-1}\mathbf{T}_{\text{virt}}. \tag{11}$$

Herein $\mathbf{A}^{-1}$ is the inverse Abel transformation operator with respect to time. For the 3D wave equation, the Abel transformation is replaced by integration with respect to the temporal variable, which results in spherical projections of the initial 3D source [25, Appendix A].

Our goal is now to relate the positive data, i.e. the circular projected virtual wave signal $\mathbf{M}_{\text{virt}}$ from Eq. (11) with the temperature signal **T**. For this purpose, we recapitulate the temperature field of Eq. (8), that is based on an arbitrary heating function $h(t)$ represented by the vector **h**:

$$\mathbf{T} = (\mathbf{K}*\mathbf{h})\mathbf{T}_{\text{virt}} = \bar{\mathbf{K}}\mathbf{T}_{\text{virt}}. \tag{12}$$

Herein (*) denotes the temporal convolution operator applied to the rows of **K**. Performing the inverse operation of Eq. (11) and substituting this into Eq. (12) yields:

$$\mathbf{T} = \bar{\mathbf{K}}\mathbf{T}_{\text{virt}} = \bar{\mathbf{K}}\mathbf{A}\mathbf{M}_{\text{virt}} = \hat{\bar{\mathbf{K}}}\mathbf{M}_{\text{virt}} \tag{13}$$

$$\text{with}\qquad \hat{\bar{\mathbf{K}}} = \bar{\mathbf{K}}\mathbf{A} = (\mathbf{K}*\mathbf{h})\mathbf{A}. \tag{14}$$

In any dimension, the circular means of a non-negative function are again non-negative. By solving Eq. (13) we can therefore incorporate the known non-negativity of the circular projections of $\mathbf{T}_{\text{virt}}$ as prior knowledge when reconstructing $\mathbf{M}_{\text{virt}}$. In order to obtain the two-dimensional virtual wave field we can apply again the Abel transformation **A** to the reconstructed virtual circular projections. We apply regularization tools to solve the inverse problems Eq. (8) and Eq. (13). For the inverse problem in Eq. (8) we use the truncated singular value decomposition (T-SVD) for regularization. To solve the inverse problem Eq. (13) we apply the alternating direction method of multipliers (ADMM).

3.1.2. Regularization

In this work we use the direct regularization method truncated T-SVD and the iterative regularization algorithm ADMM. For the sake of simplicity, the solution strategies are described for 1D temperature profiles of a single infrared camera pixel. The heat diffusion is still in 2D or 3D, where the described solution strategies are applied separately to each pixel location.

The solution using T-SVD approximates the least squares solution and its objective function is given by [30]

$$\text{minimize}\ \frac{1}{2}||\mathbf{K}\mathbf{T}_{\text{virt}} - \mathbf{T}||_2^2. \tag{15}$$

Formally we have for the virtual wave solution:

$$\mathbf{T}_{\text{virt}}^{\text{T-SVD}} = \sum_{i=1}^{k}\frac{\mathbf{u}_i^{\top}\mathbf{T}}{\mu_i}\mathbf{v}_i. \tag{16}$$

Herein, k is the regularization parameter that is estimated using the discrete *Picard plot*, where the only prior information is the noise level. $\mathbf{u}_i$ and $\mathbf{v}_i$ are orthonormal column vectors of the matrices **U** and **V**, obtained via SVD.

To incorporate the prior information positivity and sparsity we apply the ADMM algorithm, which is an efficient iterative algorithm for constrained optimization. [31]. Using ADMM the prior information sparsity is respected, because we assume that the virtual wave field $\mathbf{T}_{\text{virt}}$ is sparse. ADMM is a descendant of the *Douglas-Rachford splitting* method [32,33]. The idea is to split the objective function

$$\text{minimize}\ \frac{1}{2}||\hat{\bar{\mathbf{K}}}\mathbf{M}_{\text{virt}} - \mathbf{T}||_2^2 + \lambda||\mathbf{M}_{\text{virt}}||_1 \tag{17}$$

into two parts in order to obtain separate problems that are easier to solve. Hence, the new problem is given by:

$$\text{minimize} \quad f(\mathbf{M}_{\text{virt}}) + g(\mathbf{z}) \tag{18}$$

with $f(\mathbf{M}_{\text{virt}}) = 1/2||\hat{\mathbf{K}}\mathbf{M}_{\text{virt}} - \mathbf{T}||_2^2$, $g(\mathrm{z}) = \lambda\|\mathrm{M}_{\text{virt}}\|_1$and subject to

$$\mathbf{M}_{\text{virt}} - \mathbf{z} = \mathbf{0}. \tag{19}$$

Then we can form the *Lagrangian* with respect to Eqs. (18) and (19). To increase robustness, one adds a penalty term and an appropriate penalty parameter $\rho > 0$ to the *Lagrangian*. This approach gives the *augmented Lagrangian* and leads to the following iteration procedure to reconstruct $\mathbf{M}_{\text{virt}}$ [31]:

$$\begin{aligned} \mathbf{M}_{\text{virt}}^{k+1} &:= (\hat{\mathbf{K}}^{\top}\hat{\mathbf{K}} + \rho\mathbf{I})^{-1}[\hat{\mathbf{K}}^{\top}\mathbf{T} + \rho(\mathbf{z}^k - \mathbf{u}^k)] \\ \mathbf{z}^{k+1} &:= S_{\lambda/\rho}(\mathbf{M}_{\text{virt}}^{k+1} + \mathbf{u}^k) \\ \mathbf{u}^{k+1} &:= \mathbf{u}^k + \mathbf{M}_{\text{virt}}^{k+1} - \mathbf{z}^{k+1}. \end{aligned} \tag{20}$$

$S_{\lambda/\rho}$ is a threshold operator. In order to enforce positivity, we apply soft thresholding only to the positive entries and set the negative entries to zero. λ is a regularization parameter that is determined by the L-curve method [34].

4. Experimental results

In this section we apply the VWC to pulse thermography data based on internal heat sources. Based on the physical parameters, the time resolution and the spatial resolution we can compute the kernel matrix for T-SVD. Further, using the Abel transformation, we introduce the prior information positivity. Then a comparison of the above presented regularization tools is given. Finally, we apply F-SAFT to reconstruct the initial temperature distribution. Since the information content of $\hat{\mathbf{K}}$ is higher than for $\mathbf{K}$ we expect a significant improvement of the regularized solution for ADMM compared to T-SVD. The reconstruction of the internal heat sources is performed by F-SAFT.

4.1. Image reconstruction of internal heat sources

The test specimen is built up with graphite bars that are embedded in epoxy resin. The geometric dimensions are shown in Fig. 3a. The graphite bars are heated by laser excitation, where the laser has a wavelength of 938 ± 10 nm. As one can see in the exemplary surface temperature profiles (Fig. 4a), the laser excitation causes a volumetric heating of the epoxy resin and a surface heating of the graphite bars. Hence, the epoxy resin behaves like a semi-transparent material for the corresponding laser excitation (see Fig. 3b). The maximum power of the diode laser is 250 W and the numerical aperture is 0.22. The raise time is smaller than 10 µs and the bandwidth is greater than 50 kHz. In the experiment the laser power was 250 W and the heating time was $t_{\text{h}} = 200$ ms. The spatial laser power distribution was homogeneous over the laser spot. The laser spot diameter was approximately 40 mm. The heated graphite bars work as internal heat sources. Simultaneously, the temperature evolution is measured on the surface of the test specimen using an infrared camera. The infrared camera has an image frequency of 106 Hz in full frame modus and the noise equivalent temperature difference (NETD) is smaller than 25 mK. This camera has a cooled indium antimony (InSb) sensor, that is sensitive in the spectral range of 3.0–5.1 µm. In this spectral range the epoxy resin is opaque. Hence, we measure the temporal surface temperature at $z = 0$ and not the surface temperature of the graphite bars.

The spatial resolution is $\Delta_y = 0.098$ mm and the time resolution is $\Delta_t = 0.02$ s. Fig. 4a illustrates temporal temperature slopes for different position along the graphite bars. Fig. 4b shows spatial temperature distributions for $t = \{20,30,50\}$ s related to the corresponding maximum. For both images, the gray lines show the original data and the black lines the spatial mean value of three-hundred surface temperature slices normal to the graphite bars. As one can see, the deeper the steel rod, the lower the maximal temperature signal. This behavior is a consequence of the diffusive nature of the thermal wave.

Based on the measured surface temperature, we calculate a virtual wave field using T-SVD and ADMM. The thermal diffusivity $\alpha = 0.13\text{e}{-6}$ m^2/s was determined using the linear diffusivity fit (LDF) method [35]. The dimensionless speed of sound was set in the stable regime to $\tilde{c} = 1$. Using T-SVD we directly solve for the virtual wave field and set the benchmark for ADMM. Using ADMM, we then take into account the prior information, sparsity via the cost function Eq. (17)

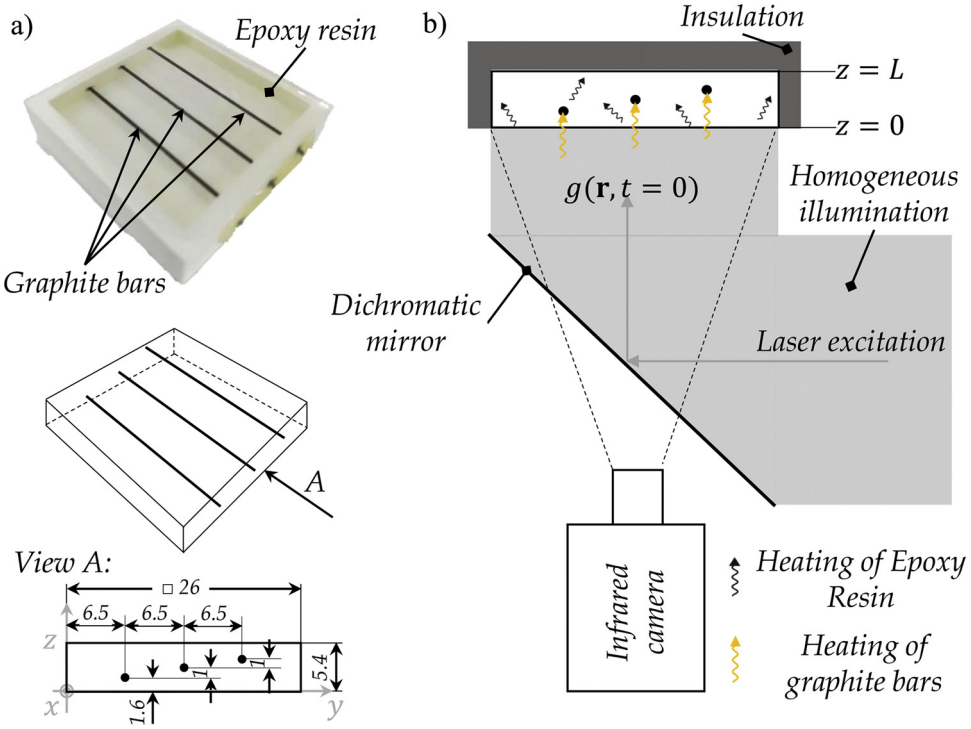

Fig. 3. (a) Test specimen built up with graphite bars, that are embedded in epoxy resin. (b) Principle sketch of the measurement set-up: The graphite bars are stimulated by laser excitation. The resulting change of the surface temperature is measured with an infrared camera.

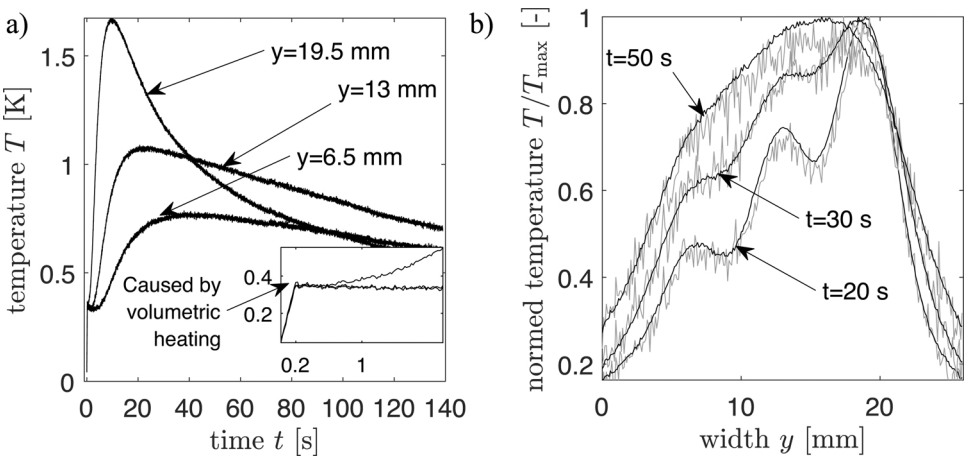

Fig. 4. (a) Temporal temperature distribution for several pixel positions. Because of the partially volumetric heating of the epoxy resin we have a sudden temperature increase at $t = 0$. (b) Spatial temperature distribution for several time stamps. The gray lines show the original data and the black lines the spatial mean value of three-hundred surface temperature slices normal to the graphite bars.

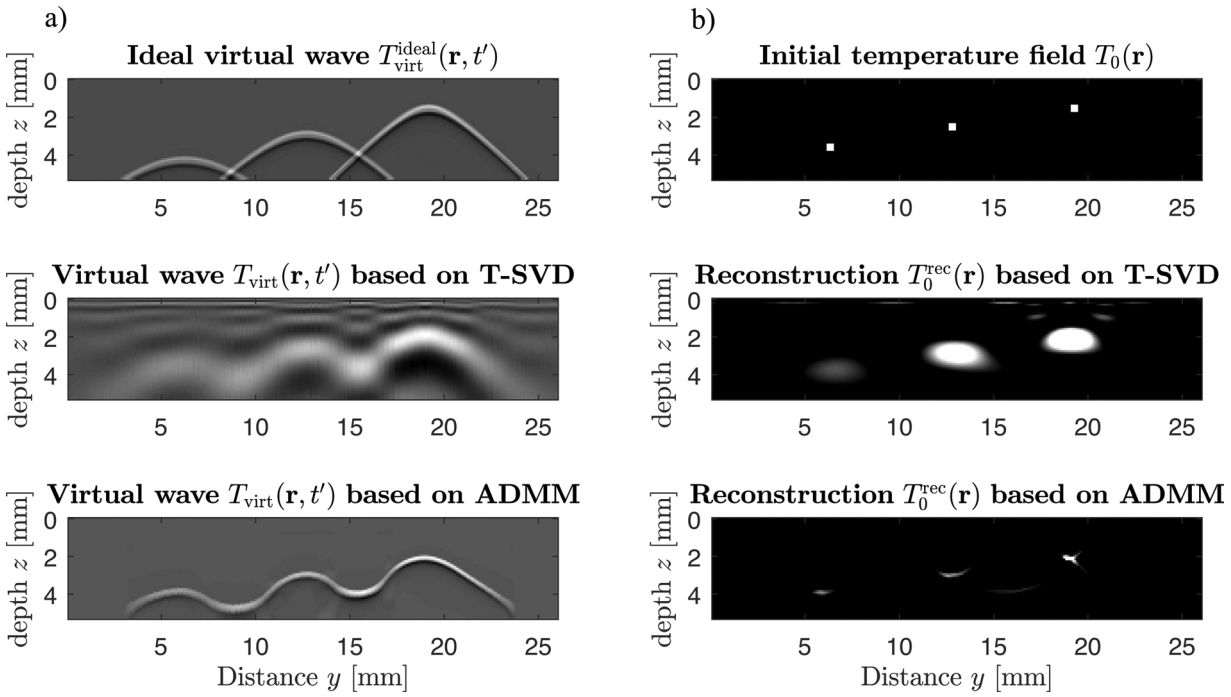

Fig. 5. (a) Comparison of the ideal virtual wave field to the reconstructed wave fields applying F-SAFT and ADMM. (b) Comparison of the initial temperature distribution and the reconstructed initial temperature distributions using T-SAFT and ADMM.

and positivity is introduced by the Abel transformation. Consequently, we calculate the regularized solution for the circular projections $\mathbf{M}_{virt}$. To calculate the virtual wave field $\mathbf{T}_{virt}$ we apply the Abel transformation to the circular projections $\mathbf{M}_{virt}$. The ideal virtual wave field and the virtual wave fields calculated by T-SVD and ADMM are illustrated in Fig. 5a. For the T-SVD, $k = 14$ singular values were respected. For the ADMM algorithm 40 iterations with a fixed penalty parameter $\rho = 0.0016$ and regularization parameter $\lambda = 7.58$ were performed. One can see, that the virtual wave field based on ADMM matches much better the ideal virtual wave field compared to T-SVD. As a consequence the image reconstruction of the internal heat sources based on ADMM exhibit a much better spatial resolution compared to T-SVD.

To highlight the process steps of VWC the result of ADMM regularization is again illustrated in Fig. 6. The left side of Fig. 6 show the results in 2D and the right side shows a 1D representation of the initial temperature field, the measured surface temperature field, the calculated virtual wave field applying ADMM, and the reconstructed initial temperature distribution applying F-SAFT. The 1D representations were obtained by evaluating the corresponding 2D fields at $y =$ {6.2,12.85,19.25} mm (see different line styles). The evaluation at y differ from the simulation because of inaccuracy in the manufacturing of the specimen. Especially, for the 1D representation of the virtual wave, we see the characteristics of 2D wave propagation. Compared to the results obtained by simulation (Fig. 2e), the experimental results (Fig. 6d) show non-symmetric rods.

For simulated data we used a homogeneous material with a certain spatial initial temperature distribution (Fig. 2a). In the experiment we see an influence caused by the volumetric heating of the semi-transparent material that have different thermophysical properties (epoxy resin and graphite). Hence, we have some balancing processes at the interface of these two materials. Consequently, we expect that the non-proper heating in the experiment affect a symmetric reconstruction of the rods.

5. Conclusions

In this work an application of the VWC for thermographic image reconstruction based on multidimensional temperature data was

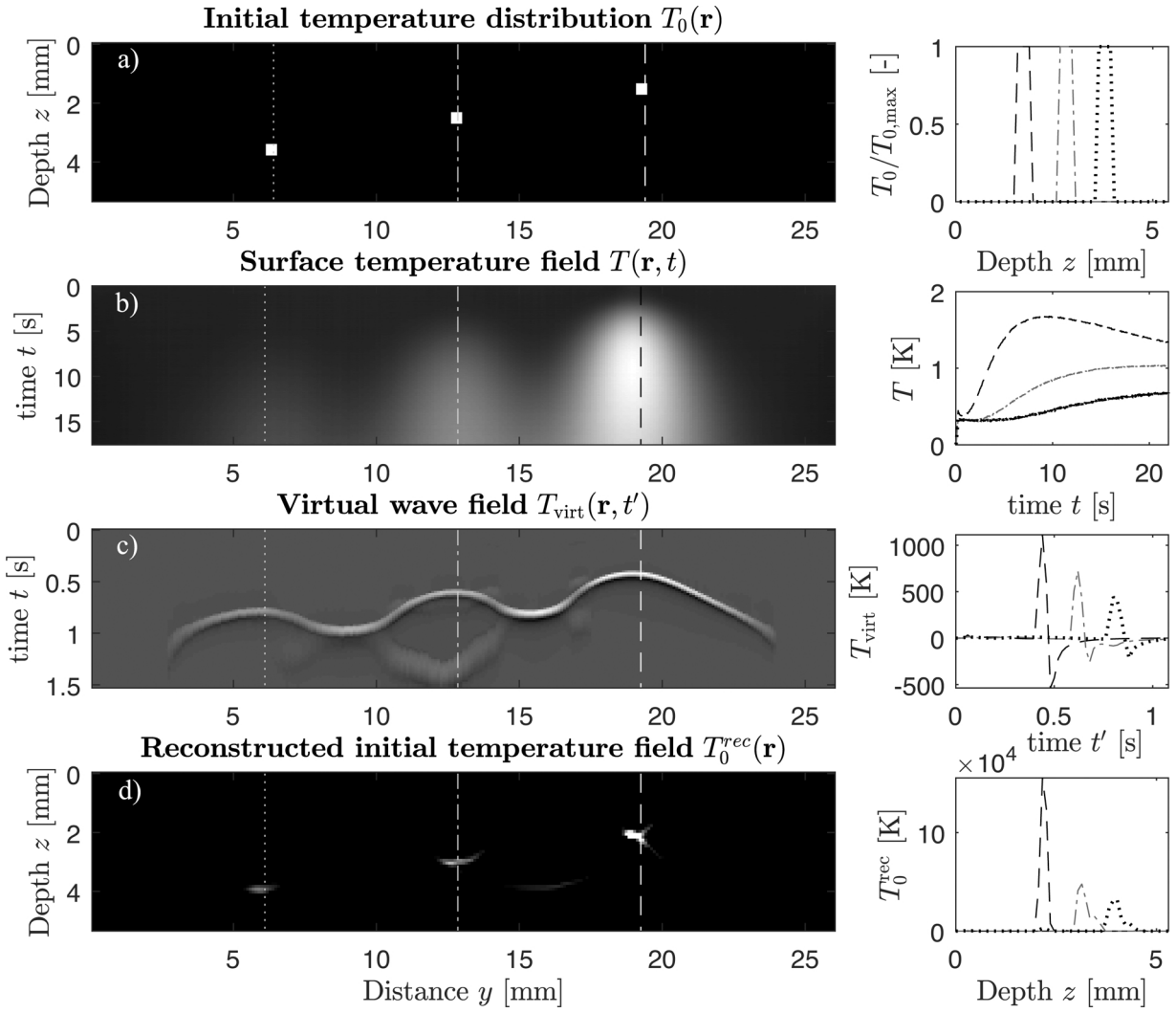

Fig. 6. Process steps of VWC based on measured data with internal heat sources: (a) initial temperature distribution 2D (left) and 1D (right) at $y = \{6.2,12.85,19.25\}$ mm, (b) measured surface temperature field, (c) virtual wave field and (d) reconstructed field.

shown. We emphasize that VWC is only meaningful and different to an IHCP when the reconstruction of defects is based on a multidimensional heat conduction problem. The main goal of this work was to illustrate that prior information significantly improves the regularized solution and, hence, the reconstructed field. Using T-SVD for regularization the information about measurement noise was considered in order to estimate the regularization parameter k. Using ADMM, the prior information positivity and sparsity were incorporated. For this purpose we reformulated the linear severely ill-posed inverse problem. The regularization and reconstruction results show that respecting more information about the data significantly increases the quality of the regularized solution. Due to the linearity of the heat and wave equation it is possible to employ VWC for thermo-tomography for the detection and characterization of cracks in isotropic and anisotropic media.

Conflict of interest

The authors declare that there is no conflict of interest.

Acknowledgments

The financial support by the Austrian Federal Ministry of Science, Research and Economy and the National Foundation for Research, Technology and Development is gratefully acknowledged. Furthermore, this work has been supported by the project multimodal and in-situ characterization of inhomogeneous materials (MiCi), by the Federal Government of Upper Austria and the European Regional Development Fund (EFRE) in the framework of the EU-program IWB2020. Financial support was provided by the Austrian Research Funding Association (FFG) under the scope of the COMET programme within the research project “PhotonicSensing for Smarter Processes (PSSP)” (contract #871974).This programme is promoted by BMVIT, BMDW, the Federal State of Upper Austria and the Federal State of Styria, represented by SFG. The work of MH has been supported by the Austrian Science Fund (FWF) project P30747-N32.

References

[1] R.A. Kruger, W.L. Kiser, D.R. Reinecke, G.A. Kruger, K.D. Miller, Thermoacoustic molecular imaging of small animals, Mol. Imaging 2 (2) (2003), https://doi.org/10.1162/15353500200303109 153535002003031.
[2] P. Beard, Biomedical photoacoustic imaging, Interface Focus 1 (4) (2011) 602–631, https://doi.org/10.1098/rsfs.2011.0028.
[3] L.V. Wang, S. Hu, Photoacoustic tomography: in vivo imaging from organelles to organs, Science 335 (6075) (2012) 1458–1462, https://doi.org/10.1126/science.1216210.
[4] P. Burgholzer, G.J. Matt, M. Haltmeier, G. Paltauf, Exact and approximative imaging methods for photoacoustic tomography using an arbitrary detection surface, Phys. Rev. E: Stat. Nonlinear Soft Matter Phys. 75 (4 Pt 2) (2007) 46706, https://doi.org/10.1103/PhysRevE.75.046706.
[5] P. Kuchment, L. Kunyansky, Mathematics of thermoacoustic tomography, Eur. J.

Appl. Math. 19 (2) (2008) 31, https://doi.org/10.1017/S0956792508007353.
[6] P. Burgholzer, G. Stockner, G. Mayr, Acoustic reconstruction for photothermal imaging, Bioengineering 5 (3) (2018), https://doi.org/10.3390/bioengineering5030070.
[7] M. Esposito, C. van den Broeck, Second law and Landauer principle far from equilibrium, EPL (Europhys. Lett.) 95 (4) (2011) 40004, https://doi.org/10.1209/0295-5075/95/40004.
[8] P. Burgholzer, Thermodynamic limits of spatial resolution in active thermography, Int. J. Thermophys. 36 (9) (2015) 2328–2341, https://doi.org/10.1007/s10765-015-1890-7.
[9] M.J. Rust, M. Bates, X. Zhuang, Sub-diffraction-limit imaging by stochastic optical reconstruction microscopy (storm), Nat. Methods 3 (10) (2006) 793–795, https://doi.org/10.1038/nmeth929.
[10] E. Betzig, G.H. Patterson, R. Sougrat, O.W. Lindwasser, S. Olenych, J.S. Bonifacino, M.W. Davidson, J. Lippincott-Schwartz, H.F. Hess, Imaging intracellular fluorescent proteins at nanometer resolution, Science 313 (5793) (2006) 1642–1645, https://doi.org/10.1126/science.1127344.
[11] T. Dertinger, R. Colyer, G. Iyer, S. Weiss, J. Enderlein, Fast, background-free, 3D super-resolution optical fluctuation imaging (SOFI), Proc. Natl. Acad. Sci. U. S. A. 106 (52) (2009) 22287–22292, https://doi.org/10.1073/pnas.0907866106.
[12] O.M. Viessmann, R.J. Eckersley, K. Christensen-Jeffries, M.X. Tang, C. Dunsby, Acoustic super-resolution with ultrasound and microbubbles, Phys. Med. Biol. 58 (18) (2013) 6447–6458, https://doi.org/10.1088/0031-9155/58/18/6447.
[13] K. Christensen-Jeffries, R.J. Browning, M.-X. Tang, C. Dunsby, R.J. Eckersley, In vivo acoustic super-resolution and super-resolved velocity mapping using microbubbles, IEEE Trans. Med. Imaging 34 (2) (2015) 433–440, https://doi.org/10.1109/TMI.2014.2359650.
[14] P. Zhang, L. Li, L. Lin, J. Shi, L.V. Wang, In vivo superresolution photoacoustic computed tomography by localization of single dyed droplets, Light Sci. Appl. 8 (2019) 36, https://doi.org/10.1038/s41377-019-0147-9.
[15] C. Errico, J. Pierre, S. Pezet, Y. Desailly, Z. Lenkei, O. Couture, M. Tanter, Ultrafast ultrasound localization microscopy for deep super-resolution vascular imaging, Nature 527 (7579) (2015) 499–502, https://doi.org/10.1038/nature16066.
[16] I.M. Vellekoop, A.P. Mosk, Focusing coherent light through opaque strongly scattering media, Opt. Lett. 32 (16) (2007) 2309–2311, https://doi.org/10.1364/OL.32.002309.
[17] J. Shi, Y. Tang, J. Yao, Advances in super-resolution photoacoustic imaging, Quant. Imaging Med. Surg. 8 (8) (2018) 724–732, https://doi.org/10.21037/qims.2018.09.14.
[18] T.W. Murray, M. Haltmeier, T. Berer, E. Leiss-Holzinger, P. Burgholzer, Super-resolution photoacoustic microscopy using blind structured illumination, Optica 4 (1) (2017) 17, https://doi.org/10.1364/OPTICA.4.000017.
[19] P. Burgholzer, T. Berer, J. Gruber, G. Mayr, Super-resolution thermographic imaging using blind structured illumination, Appl. Phys. Lett. 111 (3) (2017) 31908, https://doi.org/10.1063/1.4995410.
[20] P. Burgholzer, J. Bauer-Marschallinger, H. Grün, M. Haltmeier, G. Paltauf, Temporal back-projection algorithms for photoacoustic tomography with integrating line detectors, Inverse Probl. 23 (6) (2007) S65–S80, https://doi.org/10.1088/0266-5611/23/6/S06.
[21] L.V. Wang, Photoacoustic Imaging and Spectroscopy, Vol. 144 of Optical Science and Engineering, CRC Press, Boca Raton, 2009.
[22] L.J. Busse, Three-dimensional imaging using a frequency-domain synthetic aperture focusing technique, IEEE Trans. Ultrason. Ferroelectr. Freq. Control 39 (2) (1992) 174–179, https://doi.org/10.1109/58.139112.
[23] D. Lévesque, A. Blouin, C. Néron, J.-P. Monchalin, Performance of laser-ultrasonic F-SAFT imaging, Ultrasonics 40 (10) (2002) 1057–1063, https://doi.org/10.1016/S0041-624X(02)00256-1.
[24] P. Burgholzer, M. Thor, J. Gruber, G. Mayr, Three-dimensional thermographic imaging using a virtual wave concept, J. Appl. Phys. 121 (10) (2017) 105102, https://doi.org/10.1063/1.4978010.
[25] P.C. Hansen, Discrete Inverse Problems: Insight and Algorithms, Fundamentals of Algorithms, Society for Industrial and Applied Mathematics, Philadelphia, 2010.
[26] S. Lecheler, Numerische Strömungsberechnung: Schneller Einstieg in ANSYS CFX 18 durch einfache Beispiele, fourth edition, Springer Vieweg, Wiesbaden, 2017.
[27] C. Pozrikidis, Fluid Dynamics: Theory, Computation, and Numerical Simulation, Springer, New York and London, 2009.
[28] D. Finch, M. Haltmeier, Rakesh, Inversion of spherical means and the wave equation in even dimensions, SIAM J. Appl. Math. 68 (2) (2007) 392–412, https://doi.org/10.1137/070682137.
[29] G. Paltauf, R. Nuster, K. Passler, M. Haltmeier, P. Burgholzer, Optimizing image resolution in three-dimensional photoacoustic tomography with line detectors, SPIE Proceedings (2008) 685621, https://doi.org/10.1117/12.763161.
[30] P.C. Hansen, Rank-Deficient and Discrete Ill-Posed Problems: Numerical Aspects of Linear Inversion/Per Christian Hansen, SIAM Monographs on Mathematical Modeling and Computation, SIAM, Philadelphia, PA, 1998.
[31] R.C. Aster, B. Borchers, C.H. Thurber, Parameter Estimation and Inverse Problems, third edition, Elsevier, Amsterdam, 2018.
[32] S. Boyd, Distributed optimization and statistical learning via the alternating direction method of multipliers, Found. Trends Mach. Learn. 3 (1) (2010) 1–122, https://doi.org/10.1561/2200000016.
[33] J. Eckstein, W. Yao, Relative-error approximate versions of Douglas-Rachford splitting and special cases of the ADMM, Math. Program. 170 (2) (2018) 417–444, https://doi.org/10.1007/s10107-017-1160-5.
[34] P.C. Hansen, Regularization tools: a matlab package for analysis and solution of discrete ill-posed problems, Numer. Algorithms 6 (1) (1994) 1–35, https://doi.org/10.1007/BF02149761.
[35] G. Mayr, B. Plank, J. Sekelja, G. Hendorfer, Active thermography as a quantitative method for non-destructive evaluation of porous carbon fiber reinforced polymers, NDT & E Int. 44 (7) (2011) 537–543, https://doi.org/10.1016/j.ndteint.2011.05.012.

Gregor Thummerer studied mechanical engineering at the University of Applied Science Upper Austria both bachelor and master's degree. He is currently a Ph.D. student at the Technical University Vienna. He is a research associate at the Josef Ressel Center for Thermal Non-Destructive Evaluation of Composites at FH OÖ F&E GmbH. His main research interests are thermographic defect reconstruction and parameter estimation of composite materials.

Dr. Günther Mayr, born 1981, studied sensors and microsystems at the University of Applied Sciences Upper Austria, School of Engineering. After graduating, he worked as a research assistant at FH OÖ F&E GmbH. In 2015 he completed his dissertation at the Johannes Kepler University in the field of polymer science. Since January 2018, he is the head of the Josef Ressel Center for Thermal Non-Destructive Evaluation of Composites in Wels.

Markus Haltmeier received his Ph.D. degree in mathematics from the University of Innsbruck, Tyrol, Austria, in 2007, for research on computed tomography. He was then involved in various aspects of inverse problems as a research scientist with the University of Innsbruck, the University of Vienna, Austria, and the Max Planck Institute for Biophysical Chemistry, Göttingen, Germany. Since 2012, he is full professor with the Department of Mathematics, University of Innsbruck. His current research interests include inverse problems, signal and image processing, computerized tomography, and machine learning.

Peter Burgholzer received his Ph.D. in technical science from the Johannes-Kepler-University of Linz, Austria in 1993 with a thesis on X-ray texture measurements and anisotropy of aluminum. Since 1998 he has been lecturer at the University of Applied Sciences Upper Austria. From 2000 to 2010 he was head of the Sensor Technology Department of the Upper Austrian Research. His main working area is non-destructive testing with optical methods, especially laser ultrasound, photoacoustic imaging, and optical coherence tomography. In 2008 he could habilitate on the Technical University of Vienna in Non-Destructive Testing. Since January 2010 he is scientific director of the Christian Doppler Laboratory for Photoacoustic Imaging and Laser Ultrasonics and CEO of the Research Center for Non-Destructive Testing (RECENDT).